Journal of Alloys and Compounds 625 (2015) 296–308

Contents lists available at ScienceDirect

Journal of Alloys and Compounds

journal homepage: www.elsevier.com/locate/jalcom

Stress states in individual Si particles of a cast Al–Si alloy: Micro-Raman analysis and microstructure based modeling

Sudha Joseph [a,*], S. Kumar [a], Venkata Srinu Bhadram [b], Chandrabhas Narayana [b]

[a] Department of Materials Engineering, Indian Institute of Science, Bangalore 560 012, India
[b] Chemistry and Physics of Materials Unit, Jawaharlal Nehru Centre for Advanced Scientific Research, Jakkur P.O., Bangalore 560 064, India

ARTICLE INFO

Article history:
Received 6 May 2014
Received in revised form 1 September 2014
Accepted 31 October 2014
Available online 21 November 2014

Keywords:
Al–Si alloy
Polarized Raman technique
Finite element modeling
Si modification
Heat treatment
Stress analysis

ABSTRACT

The stress states in Si particles of cast Al–Si based alloys depend on its morphology and the heat treatment given to the alloy. The Si particles fracture less on modification and fracture more in the heat treated condition. An attempt has been made in this work to study the effect of heat treatment and Si modification on the stress states of the particles. Such understanding will be valuable for predicting the ductility of the alloy. The stress states of Si particles are estimated by Raman technique and compared with the microstructure-based FEM simulations. Combination of Electron Back-Scattered Diffraction (EBSD) and frequency shift, polarized micro-Raman technique is applied to determine the stress states in Si particles with (1 1 1) orientations. Stress states are measured in the as-received state and under uniaxial compression. The residual stress, the stress in the elastic–plastic regime and the stress which causes fracture of the particles is estimated by Raman technique. FEM study demonstrates that the stress distribution is uniform in modified Si, whereas the unmodified Si shows higher and more complex stress states. The onset of plastic flow is observed at sharp corners of the particles and is followed by localization of strain between particles. Clustering of particles generates more inhomogeneous plastic strain in the matrix. Particle stress estimated by Raman technique is in agreement with FEM calculations.

1. Introduction

The dominant mode of damage evolution in Al–Si alloy is Si particle fracture. Coarse and elongated Si particles are found to promote rapid damage evolution and this result in cast Al alloy with low ductility [1,2]. The states of stress in Si particle cause fracture, which depend on the load transfer to the stiffer particles from the complaint and plastic matrix. The particle morphology (i.e., particle size and shape), its orientation and matrix heat treatment play an important role in load transfer to the particles.

There have been a number of theories to estimate the stress states of the second phase particles in a particle reinforced composites [3–5]. These theories may not be applicable to complex shaped and highly clustered Si particles in cast Al–Si alloy. The experimental techniques which can predict the stress states in individual particles are limited in number. The neutron scattering experiments can predict the stress in the particles. However, the values obtained from these experiments are typically averaged over many thousands of particles present in different local environments. Micro-tomography [6,7] utilizing synchrotron X-ray radiation can provide stress states in individual particles of size 1–10 μm. In recent years, micro-Raman spectroscopy has been increasingly used as a technique to study the local mechanical stress in devices and structures used in microelectronics. It has the advantage of being a fast, non-destructive technique with micrometer spatial resolution. Recently, in the work of Harris et al. [8], this micro-Raman technique has been successfully implemented to study the stress states in individual Si particles of Al–Si alloy. The effects of strain and stress on the Raman frequency of the optical phonons of single crystal silicon are well known and extensively documented [9,10].

The most common procedure used in Raman stress measurement is to assume a stress state, monitor the shift in Raman peaks with the magnitude of the applied stress, and generate a calibration curve of Raman peak position against the magnitude of the applied stress. This information is then used to measure the magnitude of the stress on the same material in other loading conditions [11]. The major limitation of this technique is that it fails to resolve the tensor nature of the stress. Instead, the quantity that is obtained is a weighted average of stress components. This limitation is due to the experimental set-up which is used in the conventional back scattered micro-Raman technique, where the incident light is normal to the sample surface and neither the

* Corresponding author.

http://dx.doi.org/10.1016/j.jallcom.2014.10.207
0925-8388/

incident nor the scattered light is polarized. This particular experimental configuration cannot resolve the full stress tensor. A slight modification of this existing technique can be used to determine the in-plane stress states. Narayanan et al. [12] have proposed a polarized Raman technique to study the in-plane stress states of Si wafers which are having (1 1 1) orientation. Their procedure is adopted in this work to calculate the stress states in individual Si particles of Al–Si alloy in the as-received and loaded conditions. These would include measurements in fractured particles, whose presence can have an important effect on matrix flow, as well as in particles near fractured particles.

Alternatively, the stress states in Si particles can be predicted numerically by finite element simulations using either simple particle model or microstructure based model. Even though the simple particle models predict the stress distributions, they are unable to predict the macroscopic stress–strain behavior as accurately as the microstructure based model, since the local damage characteristics are inherently dependent on microstructure. These simple models do not include the microstructural complexities, such as, the irregular morphology of the particles, anisotropy in particle orientation and inhomogeneous spatial distribution of particles. However, these characteristics significantly influence the deformation behavior. Hence, an accurate prediction of macroscopic deformation behavior and understanding of localized damage mechanisms can only be accomplished by capturing the microstructure of the material as a basis for the model. There have been numerous studies on microstructure based modeling of particle reinforced composites [13–16].

The FEM stress analysis on Al–Si alloys has been reported by few authors [17–20]. Gall et al. [17] have studied the stress distribution near the damaged Si particle cluster. This study was carried out under cyclic loading conditions. The stress state dependent damage evolution in a cast Al–Si–Mg alloy was reported in the work of Horstemeyer et al. [18]. The effect of particle morphology on particle stress is found in the work of Saigal et al. [19] and Wang et al. [20]. However, Saigal et al. have done only the elastic analysis, but the Al matrix in the alloy will undergo elasto-plastic deformation. The above studies on Al–Si alloys are carried out using only simple particle models. There are few microstructure based modeling of Al–Si alloys to understand the fracture behavior of the alloy under tensile [21] and cyclic loading [22,23].

We have carried out a comprehensive experimental investigation to understand the effect of heat treatment [24] and Si modification [25] on particle fracture in a near-eutectic Al–Si based cast alloy. It was observed that the unmodified particles and particles oriented nearly perpendicular to the loading axis fracture more under compression. The heat treatment of the alloy also increases particle fracture. This research attempts to quantify the stress states of individual Si particles in Al–Si alloy with different microstructures under compression using Raman technique and microstructure based finite element simulations. This will reveal the effect of Si modification and heat treatment on the stress states of Si particles which in turn gives an insight into the particle fracture observed experimentally. Further, this analysis compares the experimentally and theoretically found stress values of the individual Si particles in real microstructure, which is not reported previously in the literature.

2. Experimental procedure

2.1. Material and microstructural characterization

Al–Si–Cu–Mg based cast alloys with three different types of microstructures have been taken for the analysis. The different microstructures present in the alloy are unmodified (UM) Si particles in non-heat treated (NHT) matrix, unmodified Si particles in heat treated (HT) matrix and modified (M) Si particles in heat treated matrix. The Si modification was done by controlling the processing parameters carefully. The heat treatment given to the alloy consisted of a solution treatment at 515 °C for 8 h, hot water quenching followed by aging at 175 °C for 6 h and air cooling.

The microstructural characterization of the samples was carried out under Zeiss optical microscope and field emission gun (FEG) scanning electron microscope (FEI-Sirion®) equipped with an energy dispersive X-ray spectroscopy (EDS) analysis. The samples were also subjected to Orientation Imaging Microscopy (OIM) using TSL camera under FEG scanning electron microscope. Samples for microstructural

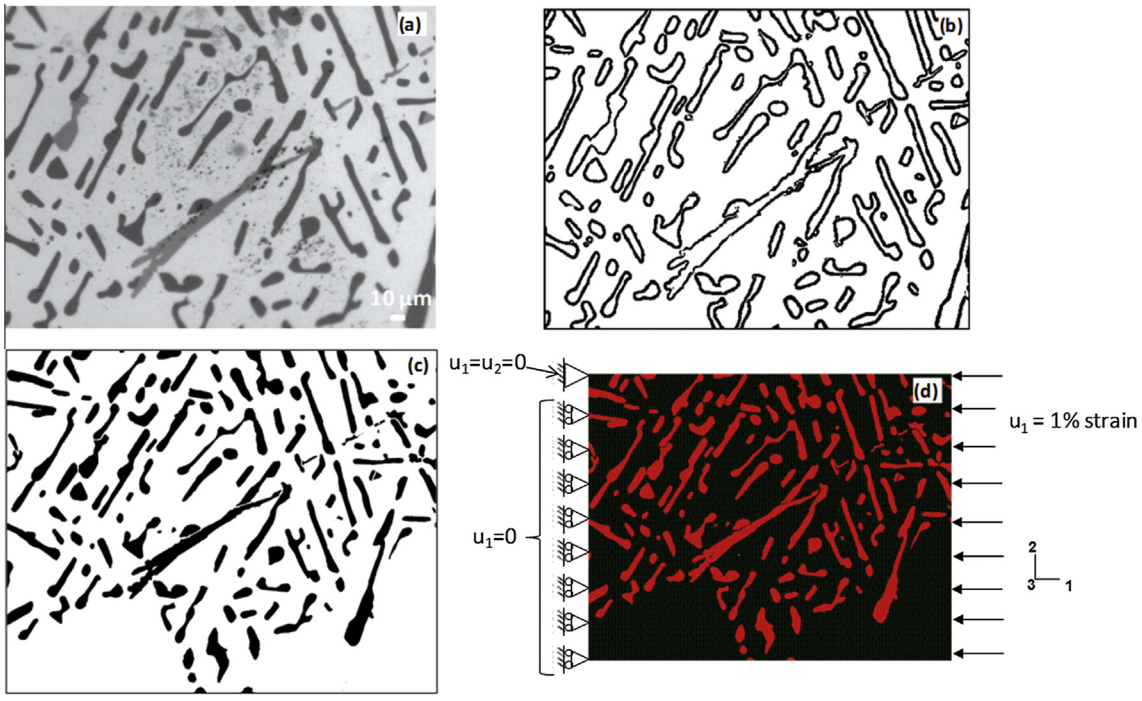

Fig. 1. Process of converting a microstructure as a basis for numerical simulation. (a) Optical image of Al–Si alloy, (b) vectorial format, (c) binary image and (d) boundary conditions of meshed microstructure under 1% compressive strain.

analysis were prepared using standard metallographic techniques. For EBSD analysis, a final polishing in the colloidal silica suspension was carried out after the standard metallographic procedure.

2.2. Compression tests

The compression tests were carried out under a displacement controlled 100 kN Dartec servo hydraulic machine (static and dynamic) upgraded with Zwick Roell software for analysis. The tests have been carried out on the three types of alloys at a quasi-static strain rate of 3×10^{-4}/s and room temperature. Bar shaped compression samples were prepared by machining the as-cast specimens to 10 mm × 10 mm cross section and 15 mm height. The samples were compressed to different strain values of 0%, 1%, 3%, 5%, 8%, 10% and 30% for microstructural examination and Raman analysis. For Raman measurements, the samples were deformed to the desired strain and unloaded, and then the measurements were made. All the analyses have been carried out on one of the polished surfaces of the specimen.

2.3. Evaluation of stress

The stress evolution in the different phases (Al matrix and Si particles) of the alloy under compression was studied by two methods, Raman technique and finite element simulations. Raman stress measurements were carried out only on Si particles, since Al is Raman inactive. Finite element simulations on real microstructures were carried out to find out the stress states in both Si particles and Al matrix. The techniques used for the study are discussed in the following sections.

Table 1
Properties assigned to Al matrix.

Property	NHT[a]	HT[b]
Yield stress, σ_0 (MPa)	237	319
Yield strain, ε_0	0.02	0.015
Constitutive relation	$\sigma = \sigma_0 (\varepsilon/\varepsilon_0)^{0.226}$	$\sigma = \sigma_0(\varepsilon/\varepsilon_0)^{0.177}$

[a] Non-heat treated.
[b] Heat treated.

2.3.1. Polarized Raman technique

2.3.1.1. Principle. When a light falls on a sample, it will be scattered in three phonon modes: two transverse and one longitudinal. These three modes have the information about all the six components of stress. In the conventional back scattered mode, all the three modes will be combined and result in overall shift of the Raman

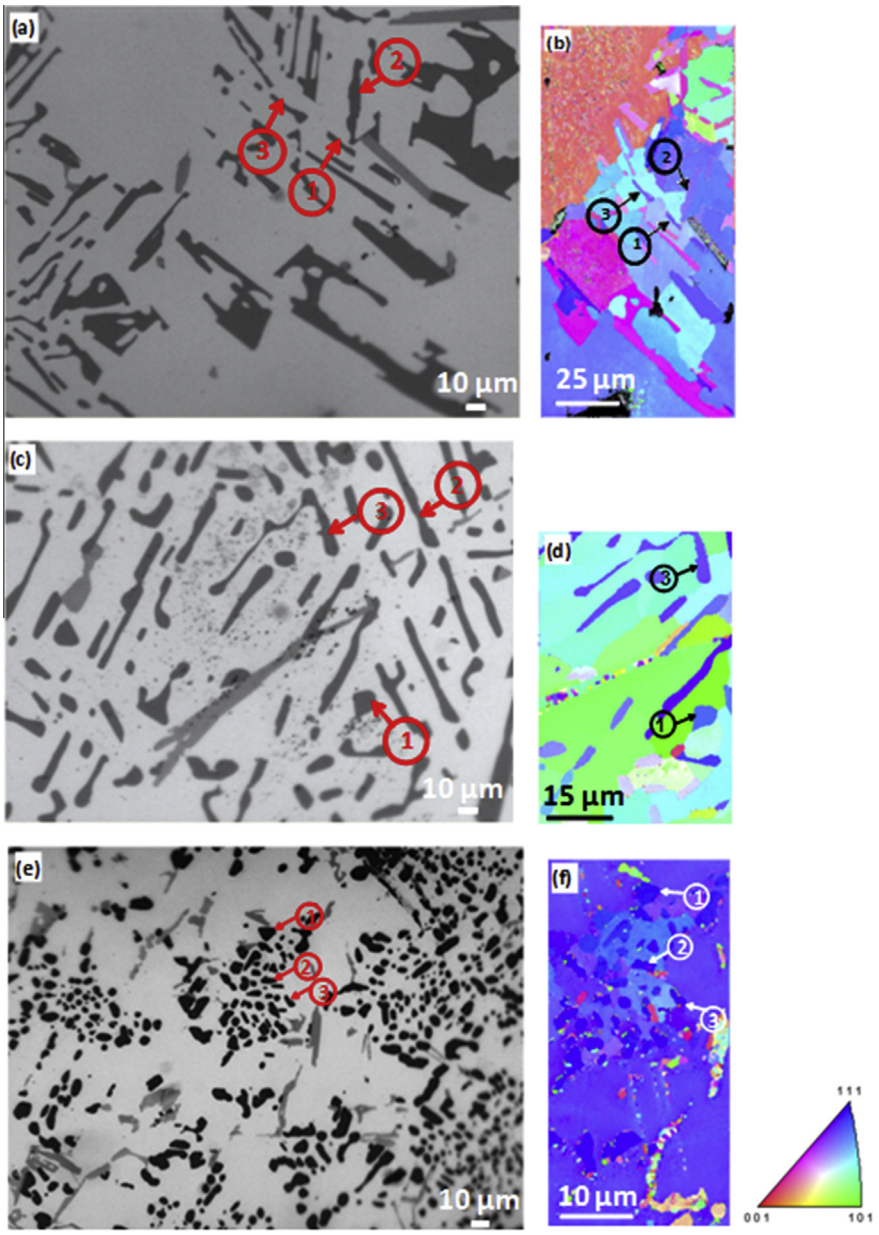

Fig. 2. Optical micrographs showing particles on which Raman analysis was carried out for (a) UM & NHT, (c) UM & HT and (e) M & HT microstructures and (b, d and f) orientation imaging maps show the (1 1 1) orientation of the particles.

peak. The separation of these peaks or getting a relative contribution from different peaks will give information about the different stress components. This can be done by polarizing the incident or scattered light.

2.3.1.2. Experiment. The Raman spectroscopy experiments were carried out in a back scattering geometry with the scattered light being captured at different polarizer angles. A custom built Raman spectrometer [26] with an excitation wavelength of 532 nm provided by a solid-state frequency-doubled Nd-YAG laser was used for the study. The laser is focused through a 50× objective lens (Nikon) to give a 1–2 μm diameter laser spot imaged on a single particle. The laser power at the sample is approximately 8 mW. Back-scattered Raman light from the sample is collimated and passed through a polarizer (Semrock) before entering the spectrometer. A charge coupled device (CCD) detects the light. The measurements were carried out in different configurations viz., parallel (0°), crossed (90°) as well as at 60° polarization. Raman spectra were collected for 120 s in order to obtain more number of counts at the peak of the Si line. Then, the peak position obtained is compared with the standard frequency of Si to calculate the shift in frequency. This shift in frequency at different polarizer angles has the information about the in-plane stress in the particles, as discussed in the next section.

2.3.1.3. Relation between frequency shift and stress states. The theory behind the Raman shift and its modulation by external loads for Si is discussed in detail by Narayanan et al. [12]. They have also experimentally observed that the normal stresses (σ_{11} and σ_{22}) in the sample affects the Raman frequency shift ($\Delta\omega$) at polarizer angles 0° and 90° and the shear stress (σ_{12}) influences the peak position at 60°. $(\Delta\omega)_0$, $(\Delta\omega)_{90}$ and $(\Delta\omega)_{60}$ represent the frequency shift at polarizer angles 0°, 90° and 60° respectively. The first two frequency shifts are found to be insensitive to shear stress. Therefore, they can be used to find the normal stresses and $\Delta\omega_{60}$ can be used to find the shear stress since it has the highest sensitivity to shear stress. The relationships between these frequency shifts and the in-plane stresses are reported in the work of Narayanan et al. [12] and are given below for the completeness of the paper.

The expressions derived for $(\Delta\omega)_0$ and $(\Delta\omega)_{90}$ are

$$(\Delta\omega)_0 = \left(\frac{K_{11}S_{11}+2K_{12}S_{12}}{2\omega_0}\right)\left[-\sigma_{22}\left(\frac{5+7p+q}{12}\right)-\sigma_{11}\left(\frac{1+3p-q}{4}\right)+\Theta\right] \quad (1)$$

$$(\Delta\omega)_{90} = \left(\frac{K_{11}S_{11}+2K_{12}S_{12}}{2\omega_0}\right)\left[\sigma_{22}\left(\frac{1+5p-q}{3}\right)+\sigma_{11}(1+p+q)\right] \quad (2)$$

where

$$p = \left(\frac{K_{11}S_{12}+K_{12}(S_{11}+S_{12})}{K_{11}S_{11}+2K_{12}S_{12}}\right) \quad (3)$$

$$q = \left(\frac{K_{44}S_{44}}{K_{11}S_{11}+2K_{12}S_{12}}\right) \quad (4)$$

$$\Theta = \frac{\alpha}{36\gamma}\left(\gamma+4\beta^2-2\sqrt{2}\sigma_{22}\beta-\left(\sqrt{2}/3\right)\alpha\beta\right) \quad (5)$$

$$\alpha = \sqrt{3}\left(\begin{array}{l}(3-6p-2q+3p^2+11q^2+2pq)\sigma_{22}^2- \\ 2\sigma_{22}\sigma_{11}(p+q-1)(3p+q-3)+3\sigma_{11}^2(p+q-1)^2\end{array}\right)^{1/2} \quad (6)$$

$$\beta = -\frac{1}{\sqrt{18}}(p+q-1)(\sigma_{22}-\sigma_{11}) \quad (7)$$

$$\gamma = \frac{1}{144}\left(\sqrt{18}\beta-6q\sigma_{22}-\alpha\right)^2+\beta^2 \quad (8)$$

where ω_0 is the Raman frequency of Si in the unstressed condition and is reported to be 520 cm^{-1} [27], K_{11}, K_{12}, K_{44}, S_{11}, S_{12} and S_{44} are material constants. K are referred to as phonon deformation potentials and for Si, they are reported to have values of $-1.43\omega_0^2$, $-1.89\omega_0^2$ and $-0.59\omega_0^2$ respectively [27]. S_{11}, S_{12} and S_{44} represent the elastic compliance parameters. The values of these parameters for Si have been reported as $S_{11} = -2.14\times10^{-6}\,(MPa)^{-1}$, $S_{12} = -2.14\times10^{-6}\,(MPa)^{-1}$ and $S_{44} = 12.7\times10^{-6}\,(MPa)^{-1}$ [28].

The expression for $(\Delta\omega)_{60}$ is

$$(\Delta\omega)_{60} = \left(\frac{K_{11}S_{11}+2K_{12}S_{12}}{2\omega_0}\right)\left[-\sigma_{22}\left(\frac{1-13p+5q}{24}\right)+\sigma_{11}\left(\frac{3+p+5q}{8}\right)+\frac{\Theta}{2}\right]+\chi\sigma_{12} \quad (9)$$

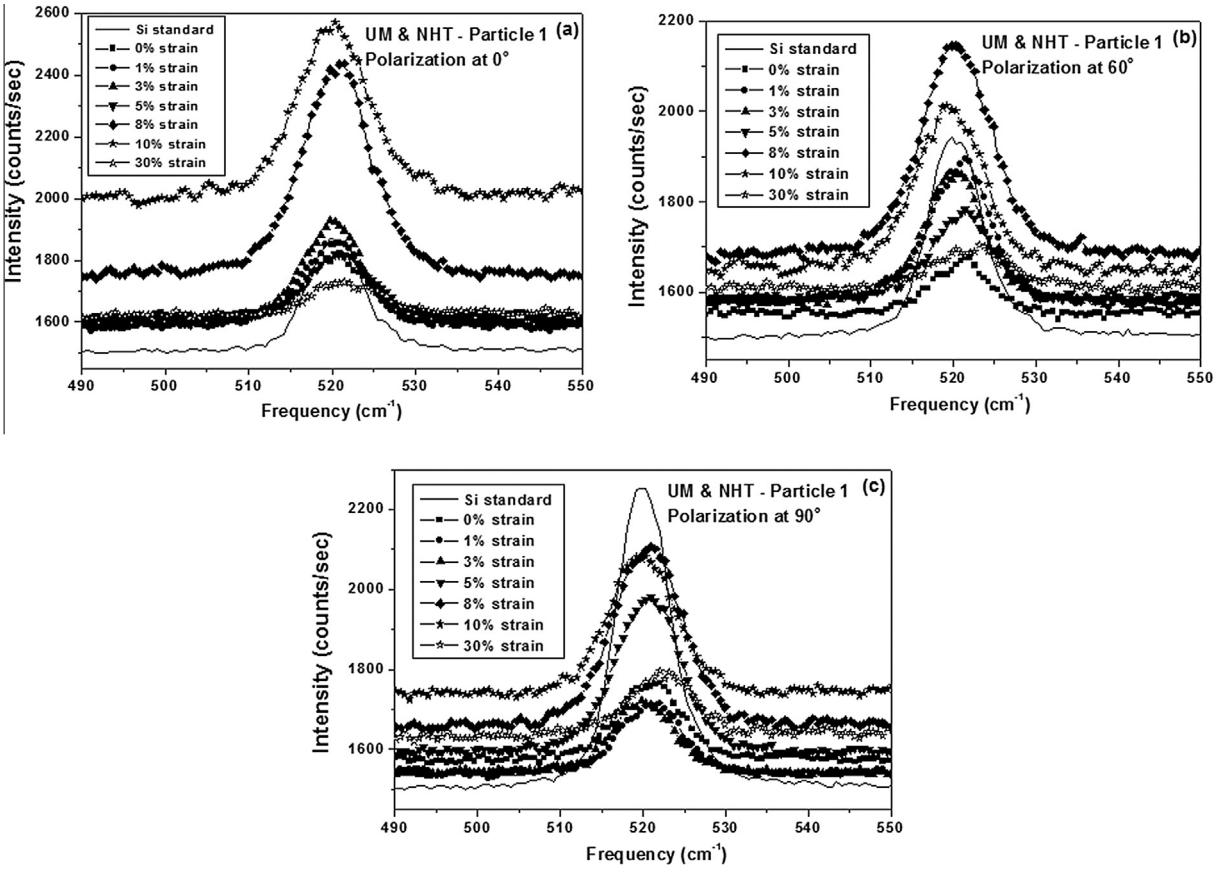

Fig. 3. Raman spectra of Si particle 1 at (a) 0°, (b) 60° and (c) 90° polarization in UM & NHT microstructure. The peaks are collected at different strain values.

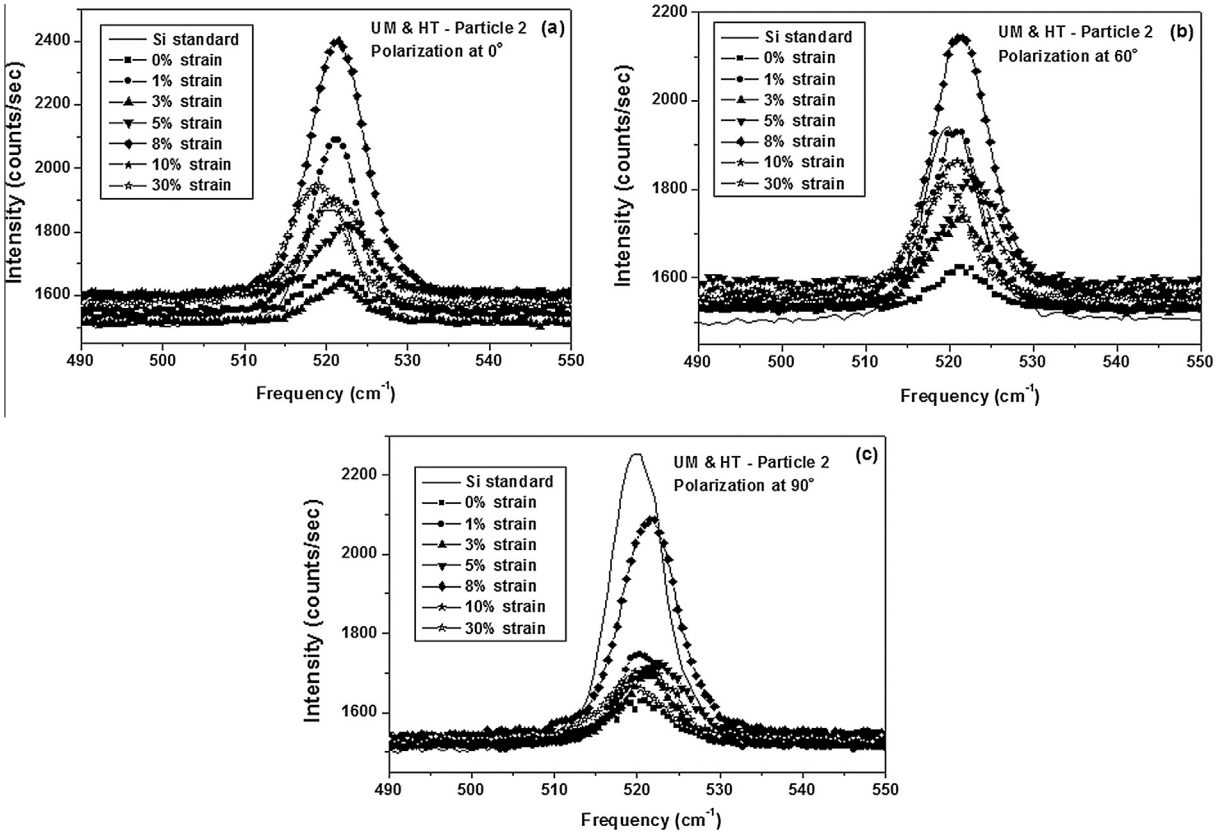

Fig. 4. Raman spectra of Si particle 2 at (a) 0°, (b) 60° and (c) 90° polarization in UM & HT microstructure. The peaks are collected at different strain values.

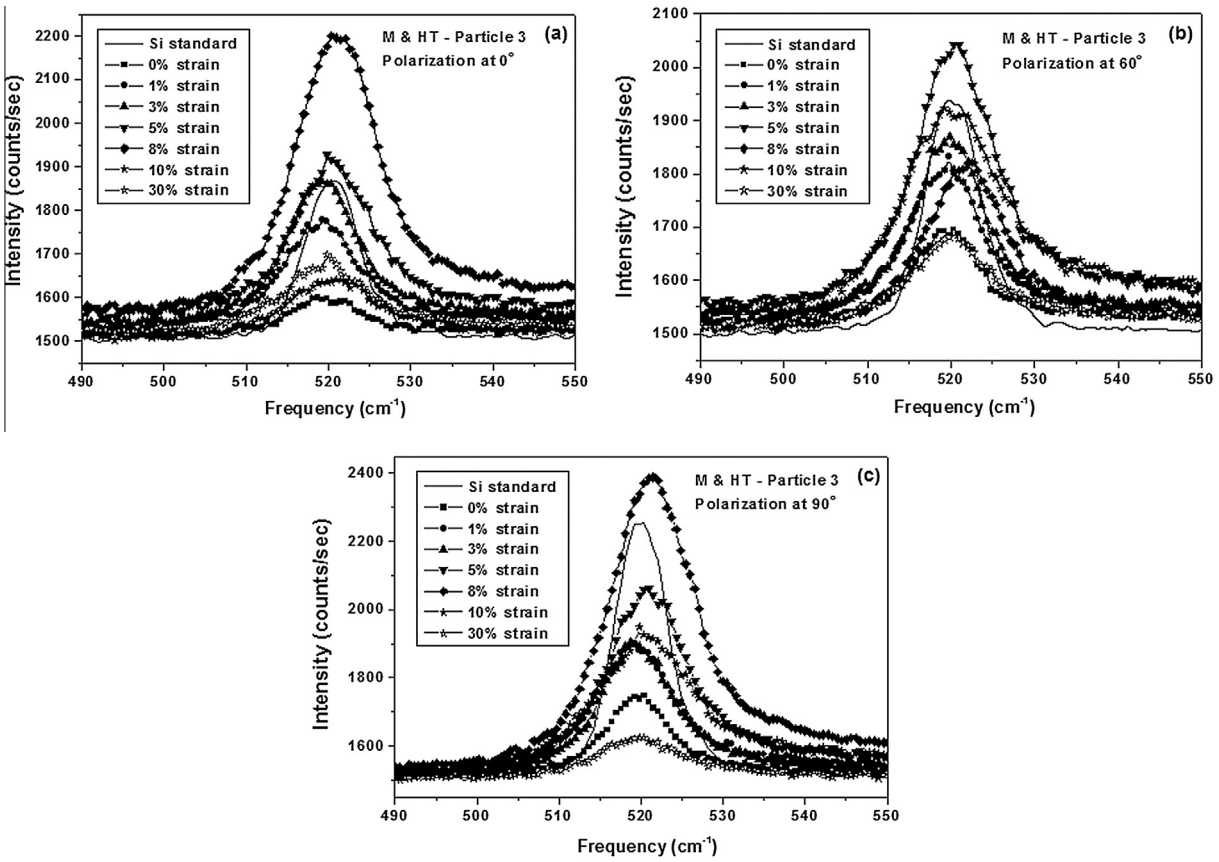

Fig. 5. Raman spectra of Si particle 3 at (a) 0°, (b) 60° and (c) 90° polarization in M & HT microstructure. The peaks are collected at different strain values.

where

$$\chi = \frac{\sqrt{3}K_{11}S_{11}\mu}{72\omega_0 q^2(1+p+\mu)^2}\left(\rho - 2\sqrt{2}q\mu + 4p - 2q^2\right)\left[\rho + 2\left(\sqrt{2}+\sqrt{6}\right)q(p+1) - 2\sqrt{6}q\mu + 2q^2\right] \quad (10)$$

$$\rho = (p^2 - p\mu + \mu - 1) \quad (11)$$

$$\mu = (1 - 2p + p^2 + 2q^2) \quad (12)$$

and p, q, Θ are defined in Eqs. (3)–(5). Once the values of σ_{11} and σ_{22} are determined from Eqs.(1) and (2), the value of the shear stress component can be determined from Eq. (9).

Since this stress analysis is applicable only to (1 1 1) type Si particles, first the crystallographic orientation of a large number of eutectic Si particles was examined with EBSD in order to identify the particles with orientations close to (1 1 1). Then, the Raman experiments were carried out on those (1 1 1) type Si particles.

2.3.2. Microstructure based finite element modeling

Actual microstructures from optical or scanning electron microscope can be incorporated into the FEM analysis. The process for conducting the analysis is shown in Fig. 1, where the optical image is converted into binary image. Then the different phases in the binary image are grouped based on their gray scales and meshed using Object Oriented Finite element program (OOF) [29]. The output from the OOF program is then analyzed by Abaqus standard. The experimentally obtained stress–strain properties are assigned to the Al matrix, which are shown in Table 1. These values are obtained by micro-hardness tests at a quasi-static strain rate of $3 * 10^{-4}$/s and RT. The Young's modulus E_{Al} and Poisson's ratio v of the Al matrix are 70 GPa and 0.3, respectively. The isotropic linear elastic properties is assigned to Si particles with Young's modulus E_{Si} = 130 GPa and Poisson's ratio v = 0.28 [17]. Then the meshed microstructure was subjected to a uniaxial compressive displacement of 1%, 3%, 5%, 8%, 10% and 30% strain. The boundary conditions for 1% strain are shown in Fig. 1(d). The maximum principal stress in the particles and equivalent plastic strain in the matrix are calculated from FEM.

One of the challenges of using a microstructure based model is that a very large number of elements and a very refined mesh are required to conform to the heterogeneous nature of the microstructure. The larger the degree of simplification of the microstructure, the more efficient the computation is. However, it will not capture the essential features of the microstructure. Three noded triangular elements are used in this analysis. A typical number of elements in the microstructure based model is about 176,200, whereas in the simplified models, the number of elements will be only 20,400. The typical size of an element in the real microstructure based model corresponds to 0.18 μm.

3. Results

3.1. Prediction of stress states in Si particles by Raman technique

Fig. 2(a, c and e) shows the optical micrographs of UM & NHT, UM & HT and M & HT alloys. It can be seen that the particles in the unmodified alloys has plate like or complex shape, whereas the particles in the modified alloy are small and almost globular. The three particles in each alloy selected for Raman investigation are shown by arrows. The orientation imaging map (OIM) of those particles in Fig. 2(b, d and f) shows that they are having (1 1 1) orientations. The (1 1 1) orientation of particle 2 in UM & HT alloy is not shown in Fig. 2(d), but this can be seen in Fig. 7(d). As described in Section 2.3.1, the Raman signals are collected for three different polarizer angles 0°, 60° and 90° from the center of each particle. The peaks are collected after compression to the strain values of 0%, 1%, 3%, 5%, 8%, 10% and 30%.

The Raman peaks collected from particle 1 of UM & NHT, particle 2 of UM & HT and particle 3 of M & HT microstructures at different polarization and different strain values are shown in Figs. 3–5 respectively. The peaks of the standard are also shown

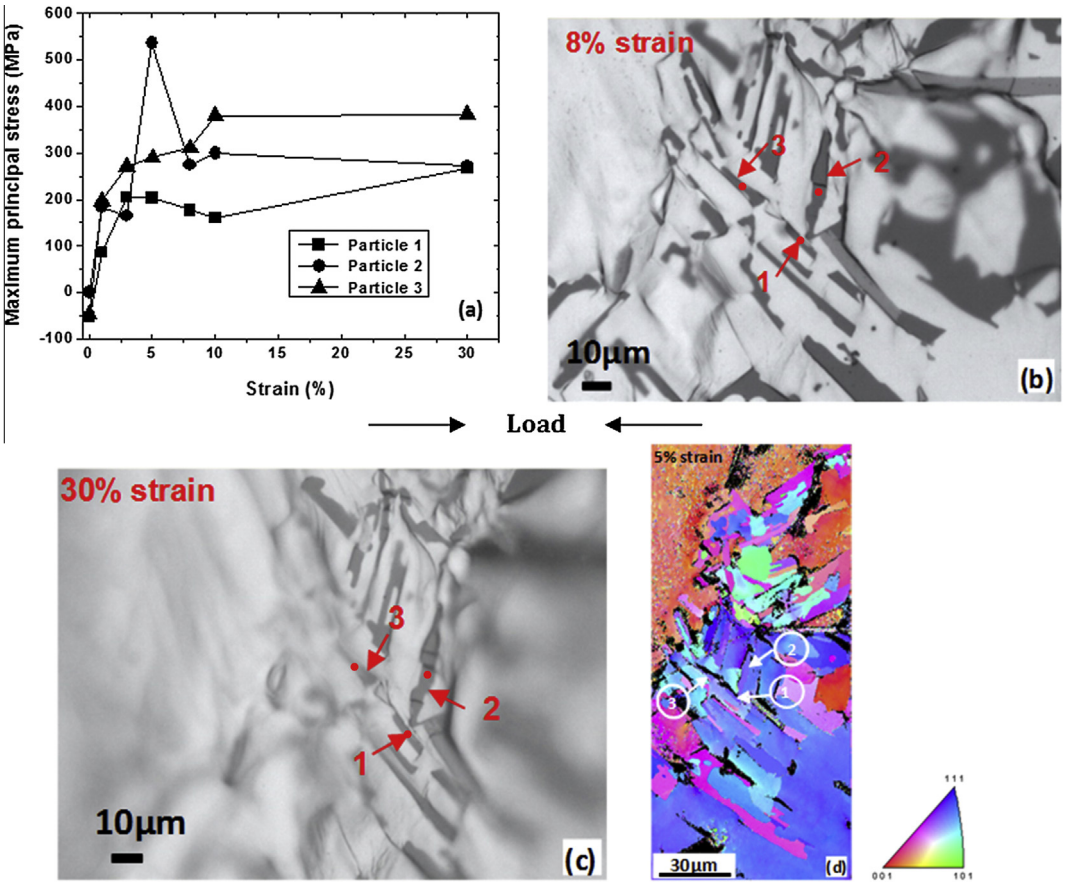

Fig. 6. (a) Si particle stress calculated by Raman technique. Optical micrographs showing (b) fracture of particle 2 at 8% strain, (c) multiple fractures of particle 2 at 30% strain and (d) orientation imaging map at 5% strain in UM & NHT microstructure.

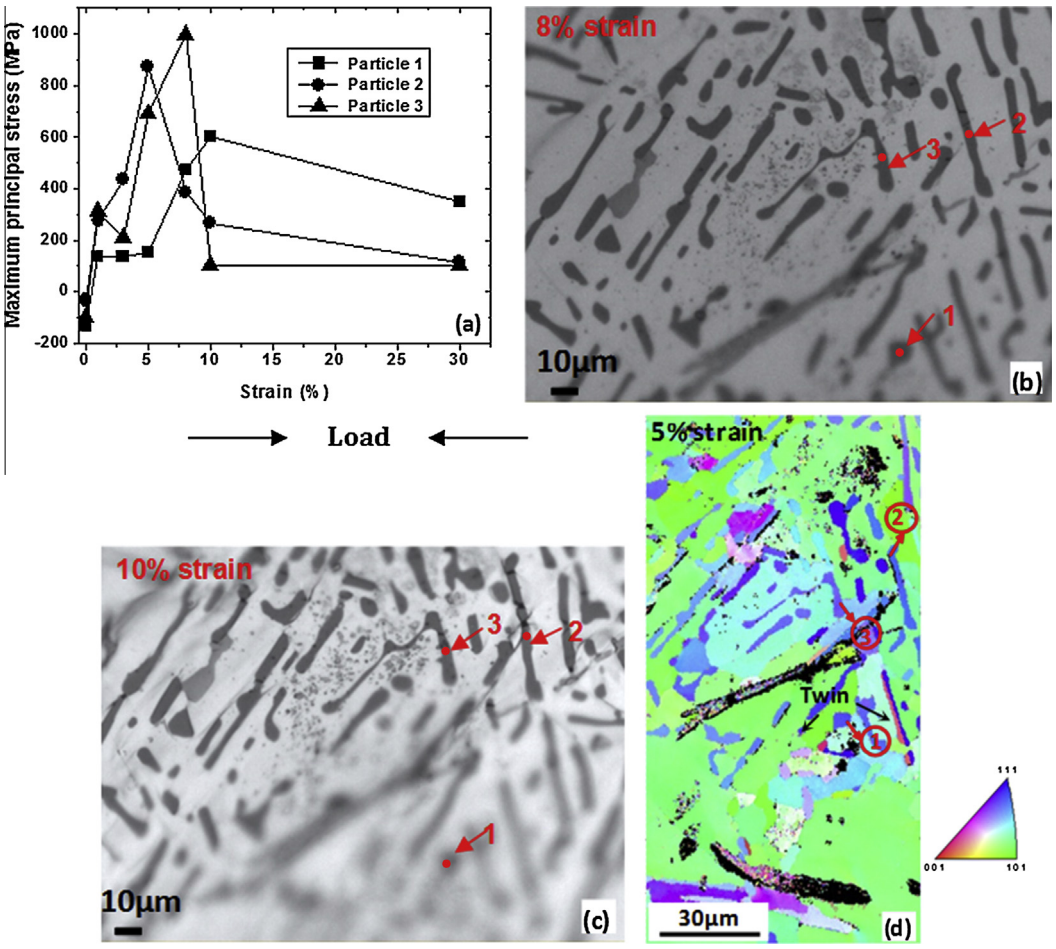

Fig. 7. (a) Si particle stress calculated by Raman technique. Optical micrographs showing (b) fracture in particle 2 at 8% strain (c) multiple fractures of particle 2 and fracture in particle 3 at 10% strain and (d) orientation imaging map at 5% strain in UM & HT microstructure.

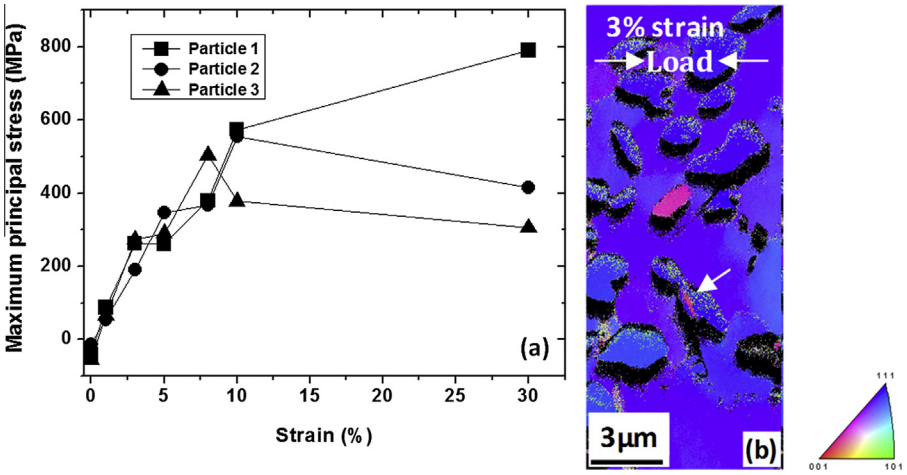

Fig. 8. (a) Si particle stress calculated by Raman technique and (b) orientation imaging map at 3% strain in M & HT microstructure. Deformation twins can be seen in Si particle at 3% strain, which is shown by arrow.

in the figures. Then, the Raman shift is calculated by comparing the peak positions with the standard after fitting the peaks to a Gaussian distribution. These Raman shift values are then used to calculate the stress in the particles by using Eqs. (1)–(12) in Section 2.3.1.3. From Eqs. (1), (2), we can calculate the stress on the particles along the loading direction (σ_{11}) and transverse to the loading direction (σ_{22}). Eq. (9) gives the in-plane shear stress (σ_{12}) on the particles. Since the maximum principal stress criterion can be used to explain fracture in brittle particles, the maximum principal stress in Si particles is calculated from these Raman stresses σ_{11}, σ_{22} and σ_{12} and is discussed in the present analysis. Hence, the term stress in the following sections refers the maximum principal

stress, unless mentioned otherwise. The stress values calculated from Raman shift is shown in Figs. 6–8 for UM & NHT, UM & HT and M & HT microstructures for the three particles in each microstructure respectively. In general, the unmodified particles show higher stress values than the modified particles and the particles in HT matrix show higher stress values than the particles in the NHT matrix. The Raman analysis of the three microstructures is discussed in detail below.

3.1.1. Particle stress in UM & NHT microstructure

The effect of strain on particle stress in UM & NHT microstructure can be seen from Fig. 6(a). From this figure, it is clear that the particle stress increases with increase in strain. The particles have stress even in the unloaded condition (i.e., at 0% strain). These are residual stresses in the particles and have values around −50 MPa. The particle stress increases with strain for all the particles except particle 2. A sudden stress drop from 535 MPa to 274 MPa for particle 2 at 8% strain is observed and it remains so for the rest of the test.

The optical micrograph of the particle is shown in Fig. 6(b) and (c). The places at which the stresses are measured on the particles are indicated by dots. A crack through the particle 2, which has a higher aspect ratio than the other two particles and is aligned nearly perpendicular to the loading axis, is observed at 8% strain (no crack was observed at lower strains) and the stress drop in Fig. 6(a) is due to particle fracture. The stress at fracture of this particle is estimated to be 535 MPa. Multiple fracture of the same particle can be seen at 30% strain from Fig. 6(c). The other two particles under study are found to be not fractured even at 30% strain. The orientation imaging map of the sample after 5% strain is shown in Fig. 6(d). The regions near the poles, sharp corners and bent regions of the particles are not indexed. This shows that those regions are heavily deformed.

3.1.2. Particle stress in UM & HT microstructure

Stress evolution and damage evolution of Si particles with the applied strain for UM & HT microstructure are shown in Fig. 7. The residual stresses in the particles are found to vary from −32 MPa to −134 MPa. There is a sudden drop in stress values at 8% strain for particle 2 and at 10% strain for particle 3, as shown in Fig. 7(a). The corresponding particle fracture behavior can be seen from Fig. 7(b) and (c). The dots on the particles in Fig. 7(b) and (c) represent the places at which the stresses are measured on the particles. Fig. 7(b) shows fracture of particle 2 at 8% strain and particle 3 is still intact. Fig. 7(c) shows multiple fracture of particle 2 and fracture in particle 3 at 10% strain. It may be noted that though both the particles have roughly the same orientation with respect to loading axis, particle 2 has a much higher aspect ratio than particle 3. The stress at fracture of the particle 2 and 3 is estimated to be 873 and 998 MPa respectively. The small globular particle 1 is found to be intact till 30% strain. The orientation imaging map in Fig. 7(d) shows the strained regions in the particle matrix interface. The deformation twins are also observed in a particle, which is shown by a black colored arrow.

3.1.3. Particle stress in M & HT microstructure

For modified particles in HT matrix, the particle stress increases with increase in strain, as shown in Fig. 8(a). The residual stresses in the modified particles vary from −13 MPa to −54 MPa. A sudden stress drop is not observed for any value of strain and the particles, which are all small and roughly globular, are also found to be intact. The orientation imaging map of the M & HT microstructure at 3% strain is shown in Fig. 8(b), in which deformation twins in Si particles can be observed.

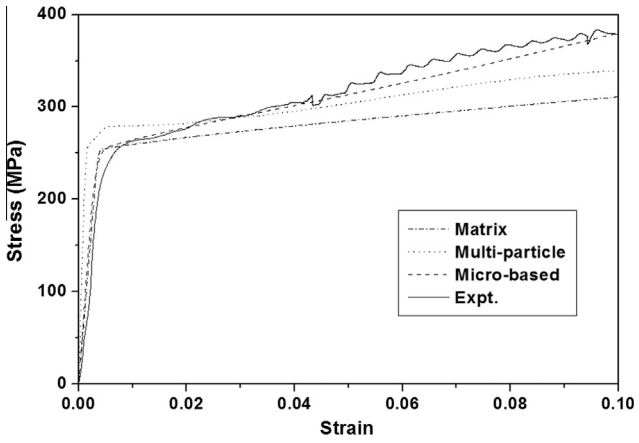

Fig. 9. Comparison of simulated stress–strain curves with experiment.

3.2. Prediction of particle stress by microstructure based FEM

Finite element analysis is carried out on the same microstructures, which have been investigated by Raman analysis, in the previous section. The simulated stress–strain curves by FEM (both multi-particle model and microstructure based model) and the experimental curve are shown in Fig. 9. The multi-particle model is generated artificially with a size of 128 mm × 128 mm pixels containing 10 vol.% of Si particles. The Si particles in the model are designed to have uniform size, spherical shape and random distribution. The microstructure based model is in excellent agreement with the macroscopically determined experimental curve, whereas the multi-particle model underestimates the stress values.

The maximum principal stress distribution in the particles obtained by microstructure based model under a uniaxial compressive strain of 1% is shown in Fig. 10. The stress distribution in the Si particles is shown for all the three microstructures. There is a uniform distribution of stress in modified particles (Fig. 10(c)), whereas the stress in the unmodified particles is higher and more complex (Fig. 10(a) and (b)). Further, the particles having higher aspect ratio take more load. Between the unmodified particles, the stress in the particles is greater in the HT condition. Higher stresses are observed in the particles having higher aspect ratio, oriented nearly perpendicular to loading axis, at the sharp corners, bent region of the particles and wherever the particles touch other particles. Therefore, these regions are more prone to crack initiation. These predictions match with the experimentally observed particle fracture characteristics, which are shown in Figs. 6 and 7(b) and (c). The particles with high aspect ratio and oriented nearly perpendicular to loading axis, and bent regions of the particles are found to fracture.

The stress distribution within the particle and the matrix immediately adjacent to the particle is shown in Fig. 11 for the particles oriented nearly perpendicular to the loading axis. This stress map is plotted along the line drawn on the particles in Fig. 10. It can be observed that the particle is under much higher stress than the matrix for all microstructures, indicating load transfer. Higher stress is observed in the unmodified than in the modified particles present in the HT matrix. The stress experienced by the particles in the NHT matrix is lower than in the HT matrix, and the NHT matrix also shows lower stress values than the HT matrix.

The evolution of equivalent plastic strain in the matrix of UM & NHT microstructure is shown in Fig. 12. It shows the onset of plastic flow at the sharp corners of the particles followed by localization of strain between particles. It has been reported that the plastic deformation is observed to concentrate near the poles of

the particles which are parallel to the loading axis [30,31] during the initial stages of deformation. However, the microstructure based model in the present study shows the initiation of plastic deformation near the poles of the particles of all orientations and the deformation is found to be greater near the complex shaped and higher aspect ratio particles. Fig. 13 compares the plastic strain in the matrix of three microstructures for 1% macroscopic strain. The plastic strain is found to be quite inhomogeneous in all microstructures. It appears to be most predominant in particle-free regions and very little in particle clustered regions. Since the matrix is allowed to shear in particle–free regions but the matrix in the particle clustered regions are subjected to higher constraints by the particles [30]. Thus, the modeling of the material using real microstructure is extremely important since all the above

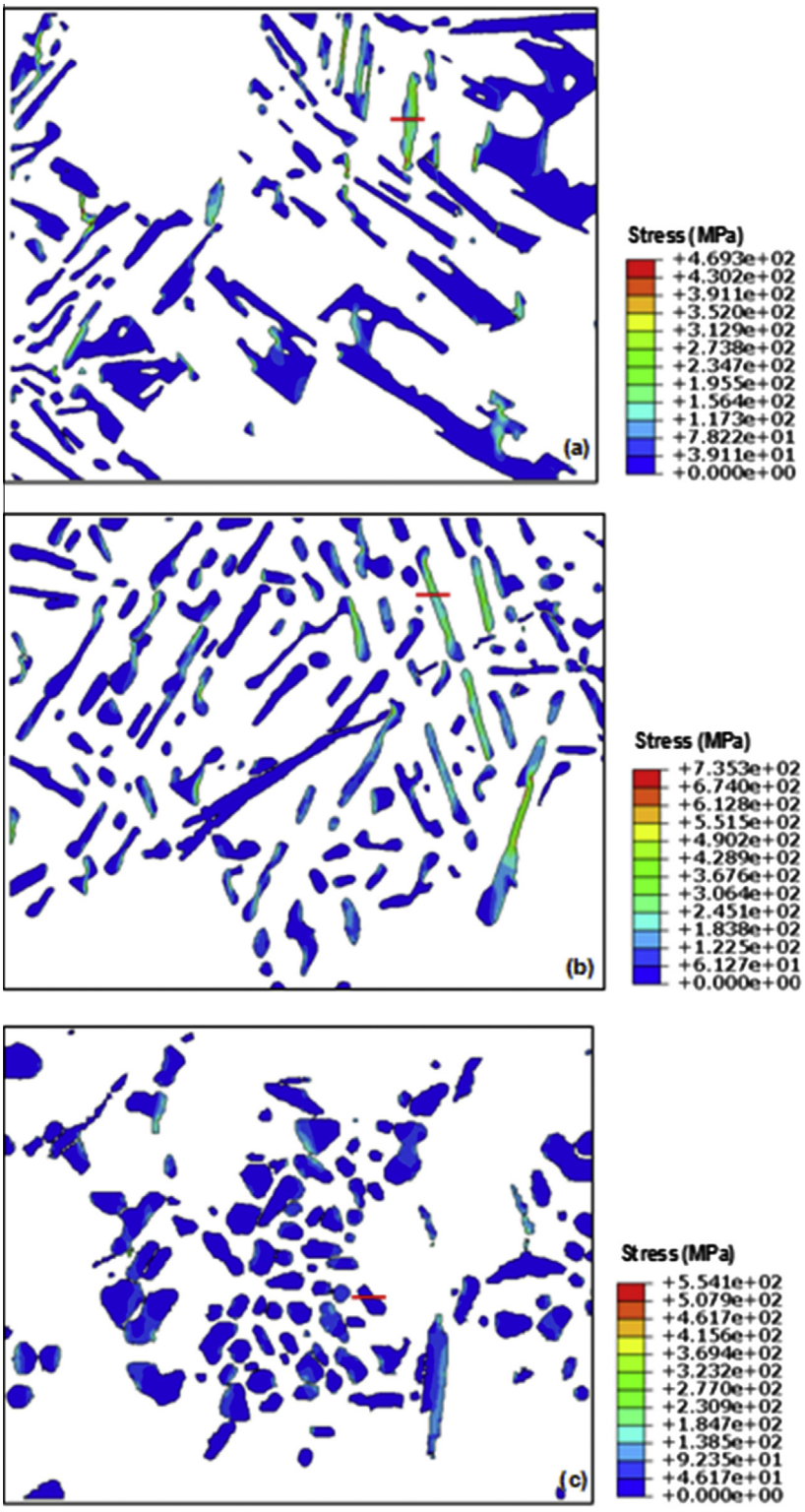

Fig. 10. Stress distribution in Si particles of (a) UM & NHT, (b) UM & HT and (c) M & HT microstructures at 1% compression.

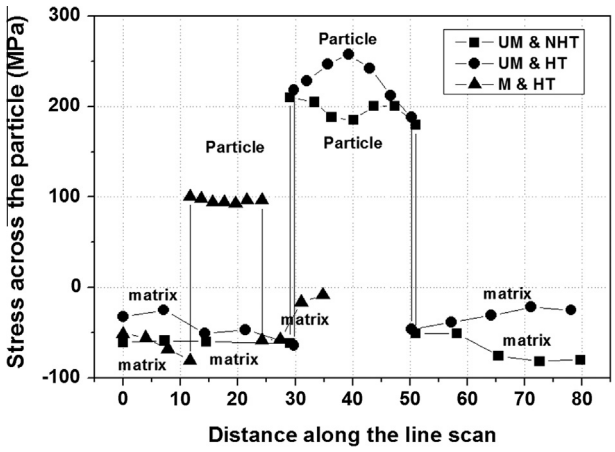

Fig. 11. Stress distribution in a particle and particle/matrix interface for three microstructures at 1% strain.

discussed fracture characteristics could not be captured by the simple particle models.

4. Discussion

The Raman technique was successfully implemented for determining the stresses in individual Si particles of an Al–Si based alloy. The measurements include the residual stress in the particles, the evolution of stress with strain and finding the stress values that cause the particles to crack. In addition, the stress in the particles is monitored after fracture also. The Raman analysis indicates that the residual stress values of the particles in different microstructures show variation from −13 MPa to −134 MPa. These stresses are generated when the alloy is cooled from the processing temperature because of mismatch of coefficient of thermal expansion between Si particles and Al matrix. This range of stress variations are expected due to different size, shape, orientation and local distribution of Si particles. These values are not only from the surface of the particles but are average values over the depth the laser can penetrate. Harris et al. [8] also found the residual stress in Si particles in the same range, −94 MPa, in their experimental measurements and they calculated it to be in the range of −50 MPa to −150 MPa by FEM analysis of thermal misfit strains.

The particle stress increases with strain for all the microstructures, as shown in Figs. 6–8. During the initial stages of straining, the particle stress increases rapidly. On further straining, the increase in particle stress is less rapid with applied strain, almost following the work hardening flow curve of the Al–Si alloy. However, the stress level in Si particle is significantly higher than in the matrix, which has a lower elastic modulus than the particle. A considerable load transfer from the weak matrix to the strong particles is the reason for the rapid increase in particle stress at the initial stages. The increase in particle stress occurs at a much lower rate at large strains due to the occurrence of plastic relaxation and particle cracking. The particle fractures, when the particle stress reaches the fracture strength of the particle. The main application of the Raman technique is its ability to determine the stress which causes Si particle fracture. The present investigation shows that this stress value is found to be ≈500–1000 MPa. These values will change with particle morphology. A value of 600 MPa is reported in the work of Harris et al. [8] and 1000 MPa is reported in the work of Caceres [32]. Our values also fall in this range.

This increase in particle stress not only depends on the applied strain but also on particle morphology and its orientation with the loading axis. Particle stress may develop by dislocation pile ups against particles [33] or by fiber loading. When the particle size

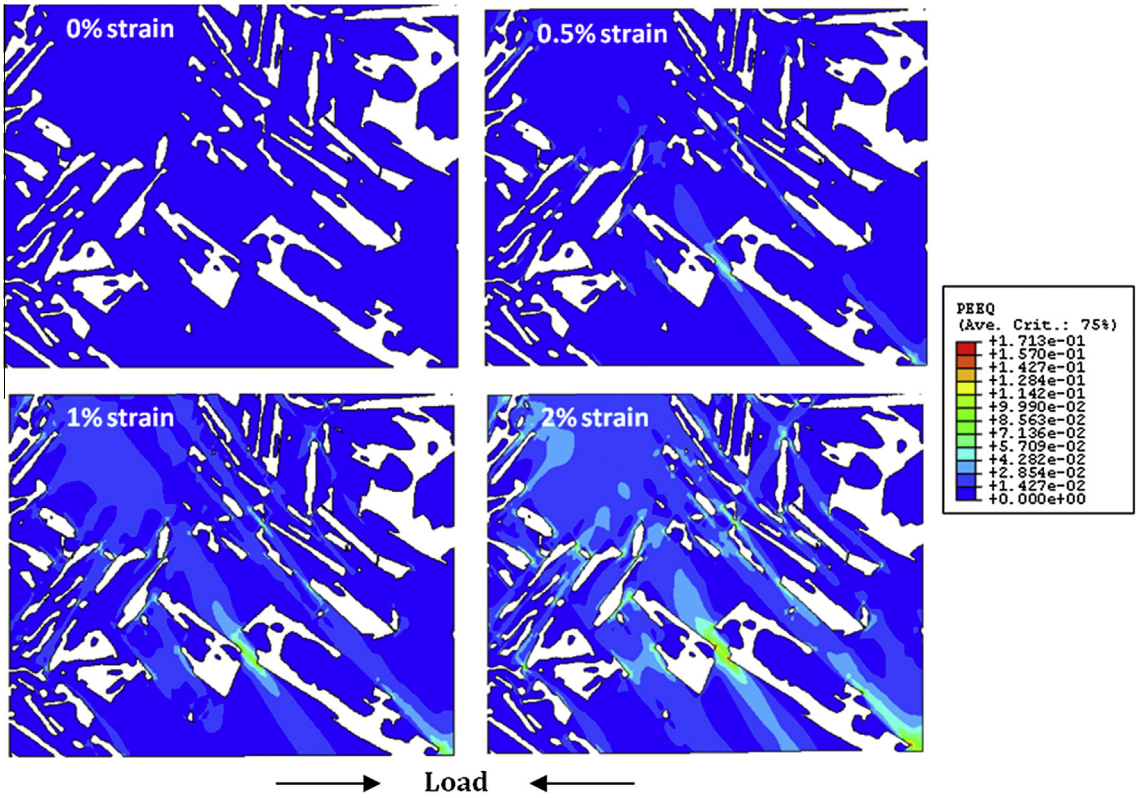

Fig. 12. Evolution of plastic strain in the matrix of UM & NHT microstructure.

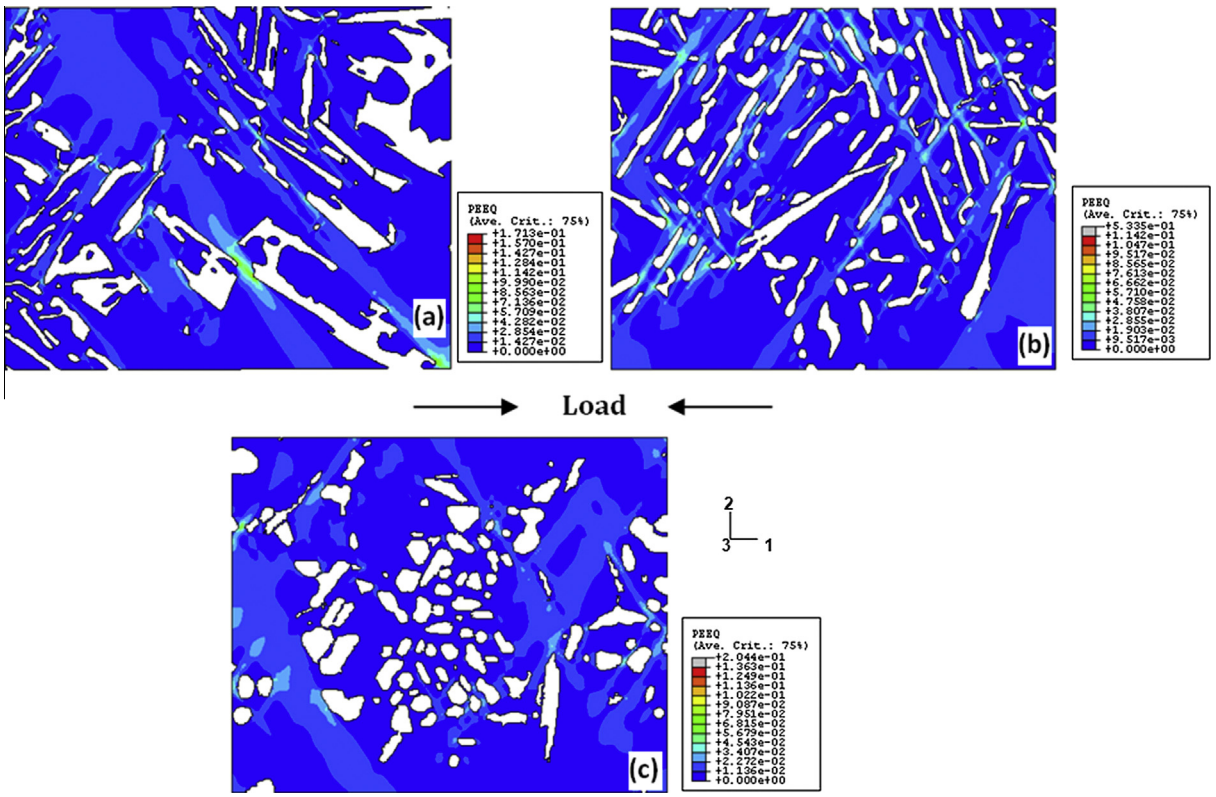

Fig. 13. Plastic strain in the matrix of (a) UM & NHT, (b) UM & HT and (c) M & HT microstructures under 1% compressive strain.

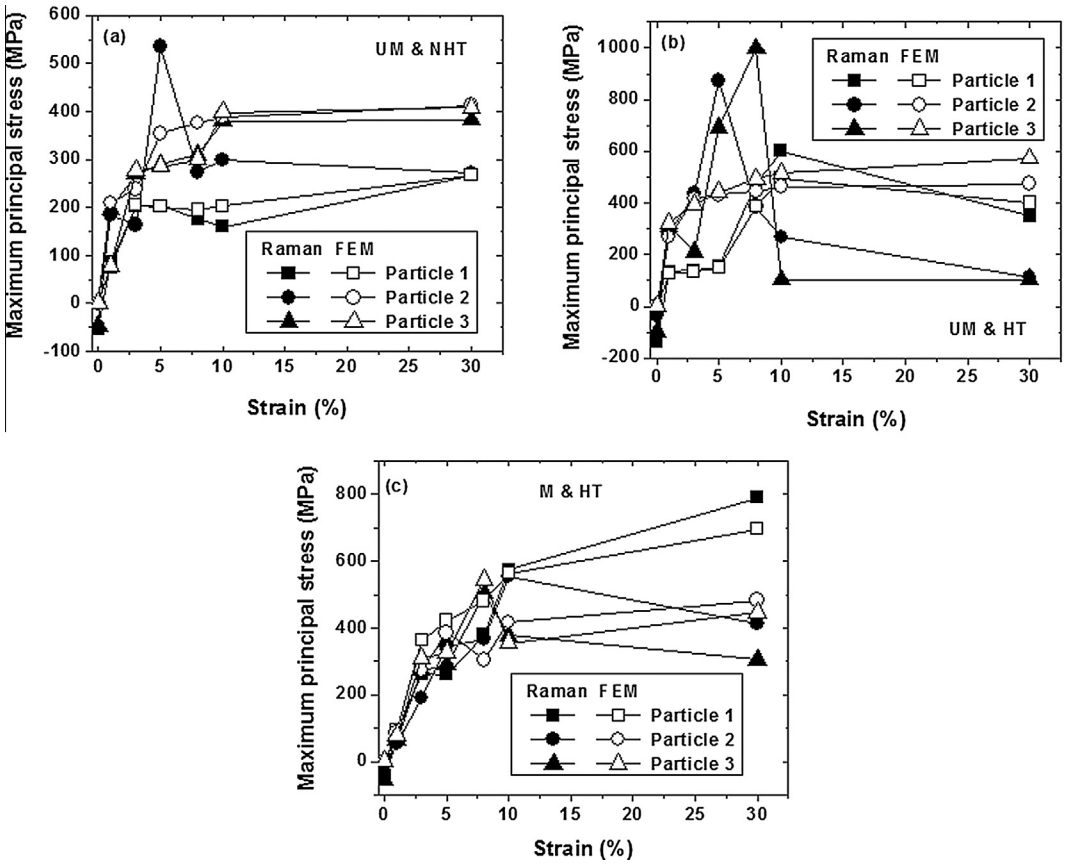

Fig. 14. Comparison of stress in the particles calculated by Raman and microstructure based FEM for (a) UM & NHT, (b) UM & HT and (c) M & HT microstructures.

is larger than the mean free path for the dislocations [34], fiber loading is responsible for particle stress. Compared to the modified alloys, the unmodified alloys show even faster increase in particle stresses, since the large and elongated particles in the unmodified alloy are subjected to fibre loading. This can be seen by comparing Figs. 7 and 8(a). The particles in the modified alloy are smaller and globular, hence the stress transfer to the particles will be lower. The modified particles are found not to fracture implying that these stress values are lesser than the fracture strength of the particles. Similarly, the lower aspect ratio particles in the UM & NHT and UM & HT microstructures are also found to be not fractured since the load transfer will be lesser in the case of lower aspect ratio particles. The stress in the particles which are oriented nearly perpendicular to the loading axis develops at a much faster rate since the tensile strain will be maximum along that direction. The particles in the HT microstructure experience greater stress, since the heat treated matrix will transfer more load to the particles. The microstructure based model also shows the same trend as predicted by Raman analysis. Thus, the particles with higher aspect ratio, oriented perpendicular to the loading direction and in the HT microstructure are more prone to fracture.

Particle fracture is also found to initiate at the sharp corners, bent regions and at the points of particle–particle contact, where the stress concentration is more, as predicted by the microstructure based model. In addition to particle fracture, particle twinning has also been observed in the alloys (Sections 3.1.2 and 3.1.3). Since the twinned regions are mechanically weak, the particle may fracture along the twinned regions on further loading.

Hence, the microcrack initiation or propagation begins with initial fracture of Si particles at low strains. Then, the microcrack can form in the matrix near the fractured particles. Once, the Al matrix yields as a result of cracking of Si particles, the highest stress in both the Si particles and Al matrix increases rapidly and results in rapid increase of particle fracture [19]. Continued straining results in localized plastic deformation of Al matrix concentrated around the fractured Si particles, which eventually leads to the formation of microcracks. Microcracks can also form near the poles and sharp corners of the particles, where the plastic deformation is concentrated (Figs. 12 and 13), as observed in microstructure based modeling. Ultimate failure will occur by the rapid linking of the microcracks which are at the right orientation.

The comparison of particle stress obtained by Raman technique and by FE calculations for the three microstructures is shown in Fig. 14. These are the maximum principal stress values in the particles. The closed symbols represent the particle stress calculated by Raman and the open symbols represent the particle stress predicted by FEM using microstructure based model. From the figure, it is clear that the stress values obtained by Raman and FEM do show agreement but not exactly the same values. This may be due to the following reasons. The residual stress values, which are present in the particles, are not included in the FEM calculations. On the other hand, Raman stress is calculated after the removal of the load. Therefore, the Raman stress will exhibit a lower stress than FEM stress by the stress corresponding to recoverable elastic strain. Once the particle fractures, the Raman calculations show sudden drop in stress values and the stresses are lower after fracture. However, FEM calculations for those particles show continuous increase in stress values even at higher strains, since the fracture criterion of the particles is not included in the FEM calculations. There is also some uncertainty in our Raman stress measurements due to the standard error in fitting the Raman spectra to a Gaussian curve, which gives an uncertainty in stress values by ±10 MPa. Despite all these reasons, a similar trend is obtained in particle stress with strain by both the Raman technique and FEM analysis.

5. Conclusions

The stress states of the individual Si particles in Al–Si based cast alloys with different microstructures are estimated by polarized Raman technique and microstructure based FEM. The maximum principal stress is used to explain the fracture characteristics of Si particles. The residual stress, the stress in the elastic–plastic regime and stress at fracture of the particle is estimated by Raman technique. The effect of heat treatment and Si modification on stress states of the particles is also studied. The following conclusions can be drawn from this work.

- The residual stress of the particles calculated by Raman technique is found to vary from −13 to −134 MPa. The stress at which particle fracture occurs is found to be 500–1000 MPa. These values would change with particle morphology. The particle stress evolution with strain mimics the flow curve of the alloy.
- FEM analysis shows that the stress distribution is uniform in modified Si and higher and more complex in unmodified Si. Stress concentration is observed at the sharp corners, bent regions and particle–particle contact point.
- The onset of plastic flow is observed at the sharp corners of the particles and is followed by localization of strain between particles. Clustering of particles generates more inhomogeneous plastic strain in the matrix.
- Both Raman and FEM analysis show that the stress evolution is more rapid in the unmodified particles. The particles oriented perpendicular to the loading axis and in the heat treated matrix show higher stress values. Hence the particles which are unmodified, oriented perpendicular to the loading axis and in a heat treated microstructure are more prone to fracture.
- Particle stress calculated by Raman and microstructure based FEM do show agreement but not exactly the same values, since the residual stress in the particles and the failure criterion of the particles are not included in the FEM calculations. On the other hand, stresses in Raman analysis are determined after unloading the sample, whereas stresses in FEM analysis are calculated in the loaded condition.

References

[1] R.C. Voigt, D.R. Bye, Microstructural aspects of fracture in A356, Trans. AFS 99 (1991) 33–50.
[2] W.M. Garrison, N.R. Moody, Ductile fracture, J. Phys. Chem. Solids 48 (1987) 1035–1074.
[3] D.S. Wilkinson, E. Maire, J.D. Embury, The role of heterogeneity on the flow and fracture of two-phase materials, Mater. Sci. Eng., A 233 (1997) 145–154.
[4] S. Yang, A.M. Gokhale, Z. Shan, Utility of microstructure modeling for simulation of micro-mechanical response of composites containing non-uniformly distributed fibers, Acta Mater. 48 (2000) 2307–2322.
[5] B.S. Majumdar, A.B. Pandey, Deformation and fracture of particulate reinforced aluminum alloy composites Part II: Modeling, Metall. Mater. Trans. A 31 (2000) 937–950.
[6] J.C. Elliott, P. Anderson, G. Davis, S.D. Dover, S.R. Stock, T.M. Breunig, A. Guevenilir, S.D. Antolovich, Application of X-ray microtomography in materials science illustrated by a study of a continuous fiber metal matrix composite, J. X-ray Sci. Technol. 2 (1990) 249–258.
[7] M. Preuss, G. Rauchs, T.J.A. Doel, A. Steuwer, P. Bowen, P.J. Withers, Measurements of fibre bridging during fatigue crack growth in Ti/SiC fibre metal matrix composites, Acta Mater. 51 (2005) 1045–1057.
[8] S.J. Harris, A. O'Neill, J. Boileau, W. Donlon, X. Su, B.S. Majumdar, Application of the Raman technique to measure stress states in individual Si particles in a cast Al–Si alloy, Acta Mater. 55 (2007) 1681–1693.
[9] E. Anastassakis, A. Pinczuk, E. Burstein, F.H. Pollak, M. Cardona, Effect of static uniaxial stress on Raman spectrum of silicon, Solid State Commun. 8 (1970) 133–138.
[10] E. Anastassakis, A. Cantarero, M. Cardona, Piezo-Raman measurements and anharmonic parameters in silicon and diamond, Phys. Rev. B 41 (1990) 7529–7535.
[11] E. Anastassakis, E. Liarokapis, Polycrystalline Si under strain: elastic and lattice-dynamical considerations, J. Appl. Phys. 62 (1987) 3346–3352.

[12] S. Narayanan, S.R. Kalidindi, L.S. Schadler, Determination of unknown stress states in silicon wafers using micro-laser Raman spectroscopy, J. Appl. Phys. 82 (1997) 2595–2602.
[13] L.-J. Zhu, W.-Z. Cai, S.-T. Tu, B.-Q. Gu, Microstructure-based computer simulation and mechanical modeling of particle-reinforced composites, International workshop on Modeling, Simulation and Optimization, 2008, pp. 396–399.
[14] N. Chawla, K.K. Chawla, Microstructure-based modeling of the deformation behavior of particle reinforced metal matrix composites, J. Mater. Sci. 41 (2006) 913–925.
[15] N. Chawla, R.S. Sidhu, V.V. Ganesh, Three-dimensional visualization and microstructure-based modeling of deformation in particle-reinforced composites, Acta Mater. 54 (2006) 1541–1548.
[16] N. Chawla, B.V. Patel, M. Koopman, K.K. Chawla, R. Saha, B.R. Patterson, E.R. Fuller, S.A. Langer, Microstructure-based simulation of thermomechanical behavior of composite materials by object-oriented finite element analysis, Mater. Charact. 49 (2002) 395–407.
[17] K. Gall, M. Horstemeyer, D.L. McDowell, J. Fan, Finite element analysis of the stress distributions near damaged Si particle clusters in cast Al–Si alloys, Mech. Mater. 32 (2000) 277–301.
[18] M.F. Horstemeyer, J. Lathrop, A.M. Gokhale, M. Dighe, Modeling stress state dependent damage evolution in a cast Al–Si–Mg aluminum alloy, Theor. Appl. Fract. Mec. 33 (2000) 31–47.
[19] A. Saigal, E.R. Fuller Jr., Analysis of stresses in aluminum–silicon alloys, Comput. Mater. Sci. 21 (2001) 149–158.
[20] A.Q. Wang, J.P. Xie, W.Y. Wang, J.W. Li, The numerical simulation of microstress for hypereutectic Al–Si alloys, Adv. Mater. Res. 211–212 (2011) 1133–1136.
[21] N. Lippmann, S. Schmauder, P. Gumbsch, Numerical and experimental study of early stages of the failure of Al/Si cast alloy, J. de Physique IV C6 (1996) 123–131.
[22] J. Fan, D.L. McDowell, M.F. Horstemeyer, K. Gall, Cyclic plasticity at pores and inclusions in cast Al–Si alloys, Eng. Fract. Mech. 70 (2003) 1281–1302.
[23] D.L. McDowell, K. Gall, M.F. Horstemeyer, J. Fan, Microstructure-based fatigue modeling of cast A356–T6 alloy, Eng. Fract. Mech. 70 (2003) 49–80.
[24] S. Joseph, A. Tewari, S. Kumar, The fracture characteristics of a near eutectic Al–Si based alloy under compression, Metall. Mater. Trans. A 44 (2013) 2358–2368.
[25] S. Joseph, S. Kumar, A systematic investigation of fracture mechanisms in Al–Si based eutectic alloy – effect of Si modification, Mater. Sci. Eng., A 588 (2013) 111–124.
[26] G.V. Pavan Kumar, C. Narayana, Adapting a fluorescence microscope to perform surface enhanced Raman spectroscopy, Curr. Sci. 93 (2007) 778–781.
[27] E.M. Anastassakis, Dynamical properties of solids, in: G.K. Horton, A.A. Maradudin (Eds.), vol. 4, North Holland, Amsterdam, 1980.
[28] G. Simmons, H. Wang, Single Crystal Elastic Constants and Calculated Aggregate Properties: A handbook, MIT, Cambridge, MA, 1971.
[29] <http://www.nist.gov/mml/ctcms/oof/>.
[30] N. Chawla, V.V. Ganesh, B. Wunsch, Three dimensional (3D) microstructure visualization and finite element modelling of the mechanical behaviour of SiC particle reinforced aluminium composites, Scripta Mater. 51 (2004) 161–165.
[31] J.N. Goodier, Concentration of stress around spherical and cylindrical inclusions and flaws, J. Appl. Mech. 55 (1933) 39–44.
[32] C.H. Caceres, J.R. Griffiths, P. Reiner, The influence of microstructure on the Bauschinger effect in an Al–Si–Mg casting alloy, Acta Mater. 44 (1996) 15–23.
[33] J-.W. Yeh, W-.P. Liu, The cracking mechanism of silicon particles in an A357 aluminium alloys, Metall. Mater. Trans. A 27 (1996) 3558–3568.
[34] M.T. Kiser, F.W. Zok, D.S. Wilkinson, Plastic flow and fracture of a particulate metal matrix composite, Acta Mater. 44 (1996) 3465–3476.